

Optimal Filtered Backprojection for Fast and Accurate Tomography Reconstruction

Chen Mu, *Student Member, IEEE*, and Chiwoo Park, *Member, IEEE*

Abstract—Tomographic reconstruction is a method of reconstructing a high dimensional image with a series of its low dimensional projections, and the filtered backprojection is one of very popular analytical techniques for the reconstruction due to its computational efficiency and easy of implementation. The accuracy of the filtered backprojection method deteriorates when input data are noisy or input data are available for only a limited number of projection angles. For the case, some algebraic approaches perform better, but they are based on computationally slow iterations. We propose an improvement of the filtered backprojection method which is as fast as the existing filtered backprojection and is as accurate as the algebraic approaches under heavy observation noises and limited availability of projection data. The new approach optimizes the filter of the backprojection operator to minimize a regularized reconstruction error. We compare the new approach with the state-of-the-art in the filtered backprojection and algebraic approaches using four simulated datasets to show its competitive accuracy and computing speed.

Index Terms—Tomographic Reconstruction, Filtered Backprojection, Optimization Algorithms.

I. INTRODUCTION

TOMOGRAPHY reconstruction is a method of reconstructing a high dimensional image with a series of its low dimensional projections from different projection angles. It has been very useful for many scientific studies, e.g., materials science [1], biological science [2] and radiology [3]. This paper is concerned about accurate and computationally efficient tomography reconstruction.

The state-of-the art in tomography reconstruction is largely categorized into two studies, analytical methods and algebraic methods. The analytical methods are based on a continuous representation of the inverse Radon Transform using the central slice theorem [4] and the computation of the discrete version of the continuous representation. A popular analytics method is the filtered backprojection (FBP) [5]. The method is computationally efficient and simple to implement. However, it is prone to amplifying observation noises. When the input projection images have high signal-to-noise ratio, the method still produces high quality reconstruction. However, when the ratio is low (in practice, this is quite common [6], [7]), the method generates a very noisy reconstruction. In addition, the reconstruction accuracy of the method deteriorates significantly when projection data are available only for a

limited number of projection angles. In practice, projection data are not available for all projection angles, e.g., in electron tomography, projections are often available in between -75 and 75 degrees of projection angles.

The algebraic methods formulate a system of linear equations that directly relate a high dimensional image to its low dimensional projections, and solves the linear equations iteratively. Depending on their modeling and iterative steps, there are many variants, the algebraic reconstruction technique (ART) [8], the simultaneous iterative reconstruction technique (SIRT) [9], [10] and the simultaneous algebraic reconstruction technique (SART) [11]. These methods perform better under observation noises and limited availability of projection data than the analytical methods, but the advantage comes with the expense of higher computational costs; the cost per iteration increases quadratically in the image size, and the slow convergence of the iterative approach requires a plenty of those expensive iterations.

Some of the recent approaches tried to combine the advantages of the analytical and algebraic methods, fine-tuning the filter used in the filtered backprojection to improve the accuracy of the filtered backprojection. The minimum residual filtered backprojection method [12] optimizes the filter to minimize the projection error of the reconstructed image. The same author also proposed another backprojection filter that approximates the algebraic method [13]. These methods are referred as to the filter-optimization approach in this paper. The accuracy of the approach does not deteriorate much as the number of projection angles decreases, but the approach is still susceptible to observation noises; this will be numerically shown in Section V. In addition, there is still a large gap in between the computation time of the filter-optimization approach and the computation time of the conventional filtered backprojection. This is because the approach needs time to solve a linear system that optimizes the filter. When data is large, the computation time could be an issue. There are simpler and faster ideas to improve the filtered backprojection, which apply denoising filters on projection data before the back projection [14], [15]. It is referred as to the denoising-and-backprojection approach in this paper. However, the simple ad-hoc ideas are not well justified theoretically or empirically.

We propose a new formulation to optimize a backprojection filter for improving the filtered backprojection. We show that the optimal filter can be achieved by finding the best Fourier domain denoising rule for given projection data, so the reconstruction can be as simple as denoising and then backprojection. Therefore, it is as fast as the conventional filtered backprojection. It appears similar to the existing denoising-and-backprojection approaches [14], [15], but there is a clear

C. Mu is with the Department of Industrial and Manufacturing Engineering, Florida State University, Tallahassee, FL, 32310-6046 USA e-mail: cm14x@my.fsu.edu.

C. Park is with the Department of Industrial and Manufacturing Engineering, Florida State University, Tallahassee, FL, 32310-6046 USA e-mail: cpark5@fsu.edu.

difference in their denoising steps. We will discuss the difference in Section III. The major contribution of this paper is to create a new filter-optimization approach for improving the filtered backprojection that is computationally efficient as the conventional filtered backprojection and as accurate as the algebraic methods. Since its solution has similarity to the denoising-and-backprojection approach, this paper also makes the linkage between the filter-optimization approach and the denoising-and-backprojection approach, which will provide methodological and empirical justifications to the denoising-and-backprojection approach.

The remainder of this paper is organized as follows. Section II describes our new filter-optimization approach, and Section III discusses the relation of the proposed approach with relevant state-of-the-arts. Section V presents numerical comparison of the proposed approach and the state-of-the-arts, which is followed by the conclusion.

II. METHODOLOGY

Let $f_0(x, y)$ denote an unknown image of interest in (x, y) -space. Let $\mathcal{R} \circ f_0(r, \theta)$ denote the line integral of the image over the line characterized by $x \cos \theta + y \sin \theta = r$,

$$\mathcal{R} \circ f_0(r, \theta) = \int_{-\infty}^{\infty} \int_{-\infty}^{\infty} f_0(x, y) \delta(x \cos \theta + y \sin \theta - r) dx dy. \quad (1)$$

Suppose that we can only measure the noisy version of $\mathcal{R} \circ f_0(r, \theta)$ that is corrupted through an additive noise process $\epsilon(r, \theta)$,

$$p(r, \theta) = \mathcal{R} \circ f_0(r, \theta) + \epsilon(r, \theta).$$

We want to recover $f_0(x, y)$ from the noisy data $p(r, \theta)$.

Let $\mathcal{F}_2 \circ f_0(u, v)$ denote the 2-D Fourier transform of $f_0(x, y)$. Equivalently, the $f_0(x, y)$ is the inverse Fourier transform of $\mathcal{F}_2 \circ f_0(u, v)$,

$$f_0(x, y) = \int_{-\infty}^{\infty} \int_{-\infty}^{\infty} \mathcal{F}_2 \circ f_0(u, v) e^{j2\pi(ux+vy)} du dv.$$

By the change of variables to (ω, θ) with $u = \omega \cos \theta$ and $v = \omega \sin \theta$, we can rewrite the inverse Fourier transform,

$$f_0(x, y) = \int_0^\pi \int_{-\infty}^{\infty} \mathcal{F}_2 \circ f_0(\omega \cos \theta, \omega \sin \theta) |\omega| e^{j2\pi w(x \cos \theta + y \sin \theta)} d\omega d\theta. \quad (2)$$

By the central slice theorem [4],

$$\mathcal{F}_2 \circ f_0(\omega \cos \theta, \omega \sin \theta) = \mathcal{F}_1 \circ p_0(\omega, \theta),$$

where $\mathcal{F}_1 \circ p_0(\omega, \theta)$ is the 1-D Fourier transform of $p_0(r, \theta)$ with respect to the first input dimension r . Therefore, equation (2) can be rewritten as

$$f_0(x, y) = \int_0^\pi \int_{-\infty}^{\infty} \mathcal{F}_1 \circ p_0(\omega, \theta) |\omega| e^{j2\pi w(x \cos \theta + y \sin \theta)} d\omega d\theta.$$

Based on the last equation, with availability of clean projection data $p_0(r, \theta)$, $f_0(x, y)$ can be reconstructed by

$$f_0(x, y) = \int_0^\pi \int_{-\infty}^{\infty} Q_{p_0}(\omega; x, y, \theta) |\omega| d\omega d\theta.$$

where $Q_{p_0}(\omega; x, y, \theta) = \mathcal{F}_1 \circ p_0(\omega, \theta) e^{j2\pi w(x \cos \theta + y \sin \theta)}$. In practice, the values of p_0 are only available at a finite number of locations (ω, θ) . Let Ω denote a finite number of the ω values and Θ denote a finite set of the θ values. The finite dimensional version of the last equation is

$$f_0(x, y) = \sum_{\theta \in \Theta} \sum_{\omega \in \Omega} Q_{p_0}(\omega; x, y, \theta) |\omega| d\omega d\theta.$$

This defines the filtered backprojection procedure [4]. When the same procedure is applied to noisy data $p(r, \theta)$, the outcome $f(x, y)$ is influenced by the noise as

$$\begin{aligned} f(x, y) &= \sum_{\theta \in \Theta} \sum_{\omega \in \Omega} Q_p(\omega; x, y, \theta) |\omega| \\ &= \sum_{\theta \in \Theta} \sum_{\omega \in \Omega} Q_{p_0}(\omega; x, y, \theta) |\omega| \\ &\quad + \sum_{\theta \in \Theta} \sum_{\omega \in \Omega} Q_\epsilon(\omega; x, y, \theta) |\omega| \\ &= f_0(x, y) + \sum_{\theta \in \Theta} \sum_{\omega \in \Omega} Q_\epsilon(\omega; x, y, \theta) |\omega|, \end{aligned}$$

where $Q_\epsilon(\omega; x, y, \theta) = \mathcal{F}_1 \circ \epsilon(\omega, \theta) e^{j2\pi w(x \cos \theta + y \sin \theta)}$ is the effect of observation noise on the reconstructed image $f(x, y)$. Note that $Q_\epsilon(\omega; x, y, \theta)$ is amplified by a factor $|\omega|$ at high frequency ω , in which noises typically exist. We propose to suppress the frequency bands of noise components by modifying $|\omega|$ to

$$|\omega| \delta(\omega \in W), W \subset \Omega,$$

where $\delta(\cdot)$ is the dirac delta function. Ideally, W should include frequency bands of signals but must exclude frequency bands of noises. For a choice of W , the resulting reconstruction $f_W(x, y)$ can be computed as

$$f_W(x, y) = \sum_{\theta \in \Theta} \sum_{\omega \in \Omega} (\mathcal{F}_1 \circ p(\omega, \theta) \delta(\omega \in W)) e^{j2\pi w(x \cos \theta + y \sin \theta)} |\omega|. \quad (3)$$

We optimize W by minimizing the regularized reconstruction error

$$\begin{aligned} \text{Minimize} \quad & \|f_W - f\|_2^2 + \lambda \mathcal{P}(f_W), \\ \text{subject to} \quad & W \subset \Omega, \end{aligned} \quad (4)$$

where $\mathcal{P}(f_W) := |W|$ is the generalization error of f_W that increases as the cardinality of W increases, and $\|f\|_2^2 := \int \int f^2 dx dy$ is the L2 norm of a function. When the value of f is only available at a finite number of (x, y) 's, the norm is the sum of the squares of the function values at the finite (x, y) locations. Since the discrete Fourier transform is an orthonormal transformation, the norm of f is equivalent to the sum of the squares of the discrete Fourier coefficients of the function,

$$\|f\|_2^2 = \sum_{\omega \in \Omega, \theta \in \Theta} |\mathcal{F}_2 \circ f(\omega \cos \theta, \omega \sin \theta)|^2.$$

Since $\mathcal{F}_2 \circ f(\omega \cos \theta, \omega \sin \theta) = \mathcal{F}_1 \circ p(\omega, \theta)$ by the central slice theorem [4], the norm is equivalent to

$$\|f\|_2^2 = \sum_{\omega \in \Omega, \theta \in \Theta} |\mathcal{F}_1 \circ p(\omega, \theta)|^2.$$

Using (3) and the definition of the norm, $\|f_W - f\|_2$ is

$$\begin{aligned}\|f_W - f\|_2^2 &= \sum_{\omega \in \Omega, \theta \in \Theta} |\mathcal{F}_1 \circ p(\omega, \theta) \delta(\omega \in W) \\ &\quad - \mathcal{F}_1 \circ p(\omega, \theta)|^2 \\ &= \sum_{\omega \in \Omega \setminus W, \theta \in \Theta} |\mathcal{F}_1 \circ p(\omega, \theta)|^2,\end{aligned}$$

and the optimization problem (4) becomes

$$\begin{aligned}\text{Minimize} \quad & \sum_{\omega \in \Omega \setminus W, \theta \in \Theta} |\mathcal{F}_1 \circ p(\omega, \theta)|^2 + \lambda |W| \\ \text{subject to} \quad & W \subset \Omega.\end{aligned}$$

The optimal solution for the problem can be achieved by the following hard thresholding rule,

$$W^* = \{\omega \in \Omega; |\mathcal{F}_1 \circ p(\omega, \theta)|^2 \geq \lambda\}. \quad (5)$$

The choice of λ is critical for the performance. We will choose λ using the generalized model description length (gMDL) model selection criterion [16], which chooses λ that minimizes the following generalization error,

$$\begin{aligned}gMDL(\lambda) &= \frac{|\Omega|}{2} \log(\|f_W - f\|_2) \\ &\quad + \frac{|W|}{2} \log \frac{\|f_W\|_2 / |W|}{\|f_W - f\|_2 / (|\Omega| - |W|)} \\ &\quad + \log |\Omega|.\end{aligned}$$

We also tried other model selection criterion such as Akaike Information Criterion (AIC) [17], [18] and Bayesian Information Criterion (BIC) [19], which did not performed better than the gMDL. Our proposed approach is referred as to the optimal filtered backprojection (oFBP).

III. INTERPRETATION OF THE PROPOSED METHODOLOGY WITH RELATION TO THE STATE-OF-THE-ART

The final output of the oFBP is

$$\hat{f}_0(x, y) = \sum_{\theta \in \Theta} \sum_{\omega \in \Omega} (\mathcal{F}_1 \circ p(\omega, \theta) \delta(\omega \in W^*)) e^{j2\pi w(x \cos \theta + y \sin \theta)} |\omega|.$$

In the expression, $\mathcal{F}_1 \circ p(\omega, \theta) \delta(\omega \in W^*)$ implies thresholding the 1-D Fourier transform of the projection data associated with projection angle θ using the thresholding rule, $\delta(\omega \in W^*)$. The same thresholding rule applies for all angle θ 's, which basically suppresses noise frequency bands, so this step can be seen as denoising. The remaining operation on $\mathcal{F}_1 \circ p(\omega, \theta) \delta(\omega \in W^*)$ is the standard backprojection. In that sense, our approach can be seen as a kind of the denoising-and-then-backprojection approach. A major difference from other denoising-and-then-backprojection approaches [14], [15] is that other approaches apply thresholding on the 2-D Fourier transform of projection data, which is expressed as

$$\mathcal{F}_2 \circ p(\omega, \nu) \delta((\omega, \nu) \in \Gamma), \Gamma \subset \Omega \times \Theta,$$

while our approach applies thresholding on the individual 1-D Fourier transforms of projection data. Therefore, in the existing approaches, different thresholding rules may apply

for projection data from different projection angles, while the thresholding rules are same for all projection angles in our approach.

On the other hands, our approach can be seen as a kind of the filter optimization approach, because its final output is derived from the solution of the optimization problem (4). Our approach places two regularizations on the solution to avoid overfitting to noises, while the existing filter optimization approaches [12], [13] do not regularize the form of the solution in their optimization. The first regularization is that the form of the filter is restricted to (6), and the second regularization is the restriction of the degrees of freedom by placing the penalty term $\mathcal{P}(f_W)$. The two regularizations ease the optimization of the filter for faster computation and also mitigate the overfit of the solution to noisy data. The existing approaches have the overfit issue. This will be shown empirically in Section V.

The aforementioned two different perspectives on our approach make the linkage in between the filter-optimization approach and the denoising-and-backprojection approach. When the backprojection filters are restricted to the form of

$$|\omega| \delta(\omega \in W), W \subset \Omega, \quad (6)$$

the filter-optimization approach is equivalent to the denoising-and-backprojection approach that performs the Fourier denoising and backprojection sequentially.

IV. IMPLEMENTATION DETAILS

This section describes the implementation details of the proposed oFBP approach. The computation of the oFBP is as simple as

- Input: discrete projection data $p(r, \theta)$ for $r \in \{r_1, r_2, \dots, r_m\}$ and $\theta \in \{\theta_1, \theta_2, \dots, \theta_n\}$.
- Step 1. For each θ_j , take the 1-D Fast Fourier transform of $p(r, \theta = \theta_j)$ and denote the Fourier coefficients by $c(\omega_i, \theta_j) := \mathcal{F}_1 \circ p(\omega_i, \theta_j)$ for $i = 1, \dots, m$ and $j = 1, \dots, n$.
- Step 2. Compute $\alpha_i = \sum_{j=1}^n c(\omega_i, \theta_j)^2$. Compute the order statistics of the α_i 's by sorting them. Let $i(k)$ denote the index of the k th largest one among them.
- Step 3. Denote $k^* = \arg \min_{k=1, \dots, m} gMDL(\lambda = \alpha_{i(k)})$.
- Step 4. $\lambda = \alpha_{i(k^*)}$ and $W^* = \{\omega_{i(1)}, \omega_{i(2)}, \dots, \omega_{i(k^*)}\}$.
- Step 5. Compute f_{W^*} using equation (3).

Steps 1 through 4 basically solves problem (5) to find the optimal filter W , and Step 5 performs the filtered backprojection with the filter.

V. NUMERICAL COMPARISONS

In this section, we numerically compare our approach (oFBP) with the most recent filtered backprojection (the MR-FBP algorithm [12]), a denoising-and-backprojection algorithm (SMF-FBP [15]), the conventional FBP, and an algebraic method (simultaneous iterative reconstruction technique or SIRT [10]). We would like to see how the compared approaches perform in terms of reconstruction accuracy and computation speed under different simulated scenarios. For the comparison, we chose four test images from the literature [12], [20], [21] as shown in 1. These images are non-noisy and serve

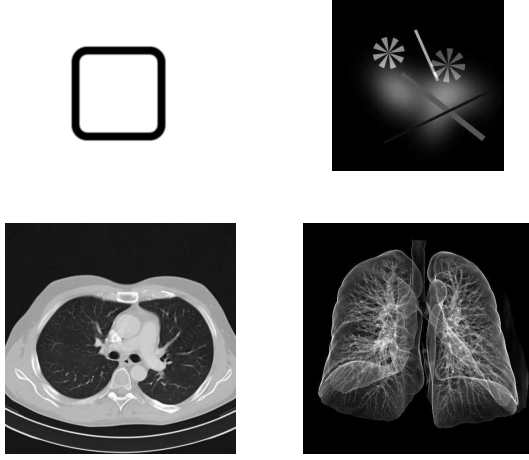


Fig. 1: Four test images of (a) a box phantom image of size 128*128 (b) a phantom image of size 256*256, (c) a thorax CT image of size 512*512 and (d) a chest CT image of size 512*512. They are all of gray scale.

as ground-truth, which is denoted by f_0 . To low dimensional projections of the four test images are computed using the Random transform. The projections are modified by adding observations noises and/or removing a part of them, before being fed to the five reconstruction methods. The reconstructed outcome is denoted by \hat{f}_0 . Different images have different image formats having different pixel ranges, e.g. for one image, those range from 0 to 1 and for one another, those range from 0 to 255. To normalize out the scaling factor, we use the following scaled mean squared error to measure the reconstruction error,

$$MSE(\hat{f}) = \frac{1}{|X||Y|} \sum_{x \in X} \sum_{y \in Y} (S \circ \hat{f}_0(x, y) - S \circ f_0(x, y))^2,$$

where S is a scaling operator with $S \circ f = (f(x, y) - \min f(x, y)) / (\max f(x, y) - \min f(x, y))$. We implemented our method, FBP, SIRT and SMF-FBP in MATLAB and used the authors' codes for the MR-FBP.

A. Comparison Under Observation Noises

To simulate noisy projection, we applied equation (1) on each of the test images and added Gaussian white noises on the results; an empirical justification of the use of the additive Gaussian noises is provided in the Appendix. Cases with different signal-to-noise ratios (SNRs) were simulated. Seven SNR values are considered, including 25, 30, 35, 40, 50, 60 and 70. For each case, the simulated data was used as inputs to each of the compared methods, and the resulting reconstruction \hat{f} was compared with the groundtruth f in terms of $MSE(\hat{f})$.

2 to 5 visualize the reconstruction results for different SNRs. TABLES I to IV show the MSE values and the computation times for different SNR levels. The MSE values and the computation times are averaged over ten replicated experiments.

TABLE I: MSEs and computation times with the first test image; each cell contains the MSE and the computation time (seconds, in parenthesis) averaged over ten replicated experiments.

SNR	25	30	40	50	60	70
oFBP (our method)	0.0419 (0.383)	0.0334 (0.383)	0.0197 (0.386)	0.0108 (0.379)	0.0107 (0.391)	0.0106 (0.379)
FBP	0.1640 (0.339)	0.1627 (0.373)	0.0394 (0.377)	0.0092 (0.377)	0.0046 (0.374)	0.0044 (0.370)
SIRT	0.0727 (1.916)	0.0479 (2.487)	0.0200 (4.541)	0.0060 (6.166)	0.0030 (6.148)	0.0026 (6.277)
MR-FBP	0.2055 (1.533)	0.2032 (1.545)	0.1767 (1.600)	0.1757 (1.565)	0.1752 (1.538)	0.1758 (1.570)
SMF-FBP	0.0533 (0.642)	0.0497 (0.342)	0.0410 (0.349)	0.0406 (0.349)	0.0401 (0.344)	0.0401 (0.361)

TABLE II: MSEs and computation times with the second test image; each cell contains the MSE and the computation time (seconds, in parenthesis) averaged over ten replicated experiments.

SNR	25	30	40	50	60	70
oFBP (our method)	0.0207 (0.527)	0.0177 (0.383)	0.0058 (0.387)	0.0017 (0.384)	0.0008 (0.383)	0.0008 (0.359)
FBP	0.1460 (0.444)	0.0798 (0.264)	0.0136 (0.256)	0.0061 (0.262)	0.0031 (0.264)	0.0031 (0.261)
SIRT	0.0300 (8.618)	0.0200 (7.863)	0.0052 (13.206)	0.0018 (13.117)	0.0018 (13.208)	0.0017 (13.138)
MR-FBP	0.1339 (3.754)	0.0666 (3.889)	0.0142 (3.748)	0.0039 (3.812)	0.0038 (4.078)	0.0036 (3.670)
SMF-FBP	0.0128 (1.660)	0.0053 (0.883)	0.0034 (0.929)	0.0032 (0.896)	0.0032 (0.890)	0.0032 (0.911)

In general, our oFBP method shows a stronger denoising ability. The differences among the compared methods becomes clearer at the highest noise level or the smallest SNR. Qualitatively, as shown in 2 to 5, the reconstruction results of the oFBP are clearer than the other competing methods. These qualitative comparisons are well supported by the MSE performance shown in TABLES I to IV. More detailed discussions follow.

1) *oFBP vs. FBP*: We included the FBP as a baseline algorithm for this comparison. The FBP used in this comparison uses the Ram-Lak filter, which magnifies noises in projection data during its reconstruction procedure. It is not

TABLE III: MSEs and computation times with the third test image; each cell contains the MSE and the computation time (seconds, in parenthesis) averaged over ten replicated experiments.

	25	30	40	50	60	70
oFBP (proposed method)	0.0115 (1.312)	0.0106 (0.681)	0.0057 (0.710)	0.0024 (0.681)	0.0022 (0.684)	0.0020 (0.695)
FBP	0.1140 (1.309)	0.0980 (0.697)	0.0483 (0.669)	0.0118 (0.681)	0.0045 (0.671)	0.0045 (0.681)
SIRT	0.0305 (27.022)	0.0205 (23.861)	0.0065 (52.448)	0.0025 (52.176)	0.0025 (52.063)	0.0025 (52.067)
MR-FBP	0.0913 (13.579)	0.0717 (12.992)	0.0240 (13.094)	0.0063 (13.011)	0.0044 (13.168)	0.0039 (13.327)
SMF-FBP	0.0180 (6.013)	0.0070 (3.329)	0.0046 (3.338)	0.0044 (3.343)	0.0043 (3.345)	0.0043 (3.347)

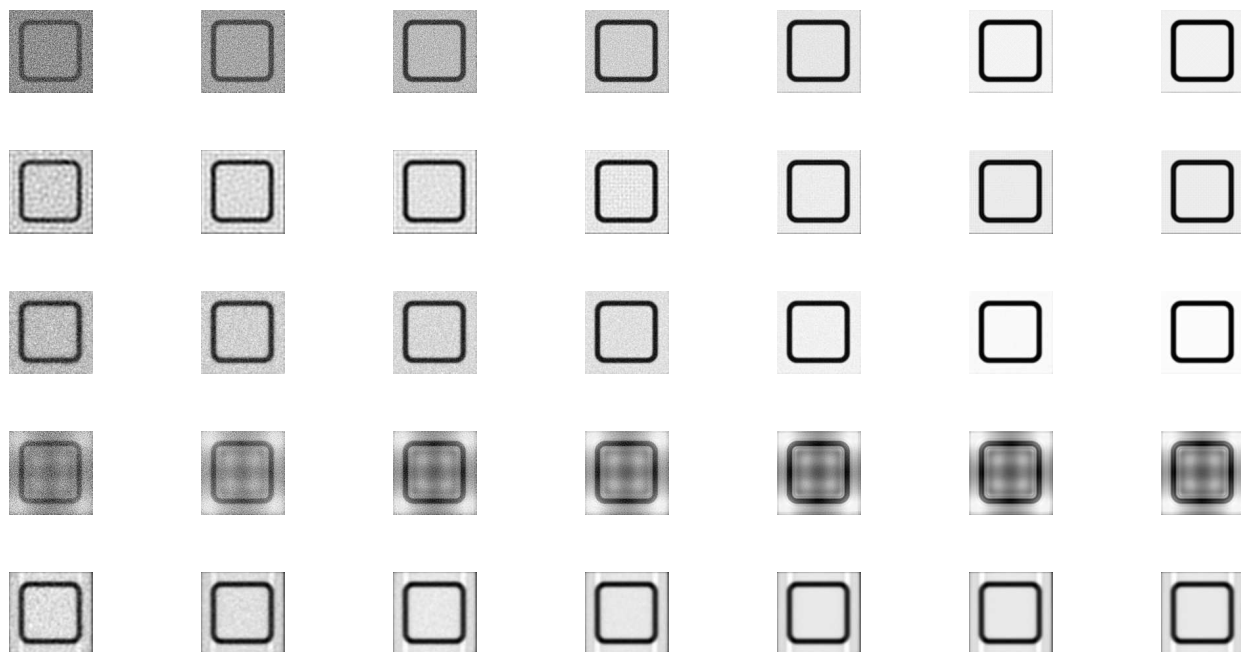


Fig. 2: Results with the first test image. The first row through the fifth row of the images correspond the reconstruction results from the oFBP, oFBP, SIRT, MR-FBP and SMF-FBP method respectively, and different columns of the images represent the results with different signal-to-noise ratios, 25, 30, 35, 40, 50, 60 and 70 from the leftmost to the rightmost column.



Fig. 3: Results with the second test image.

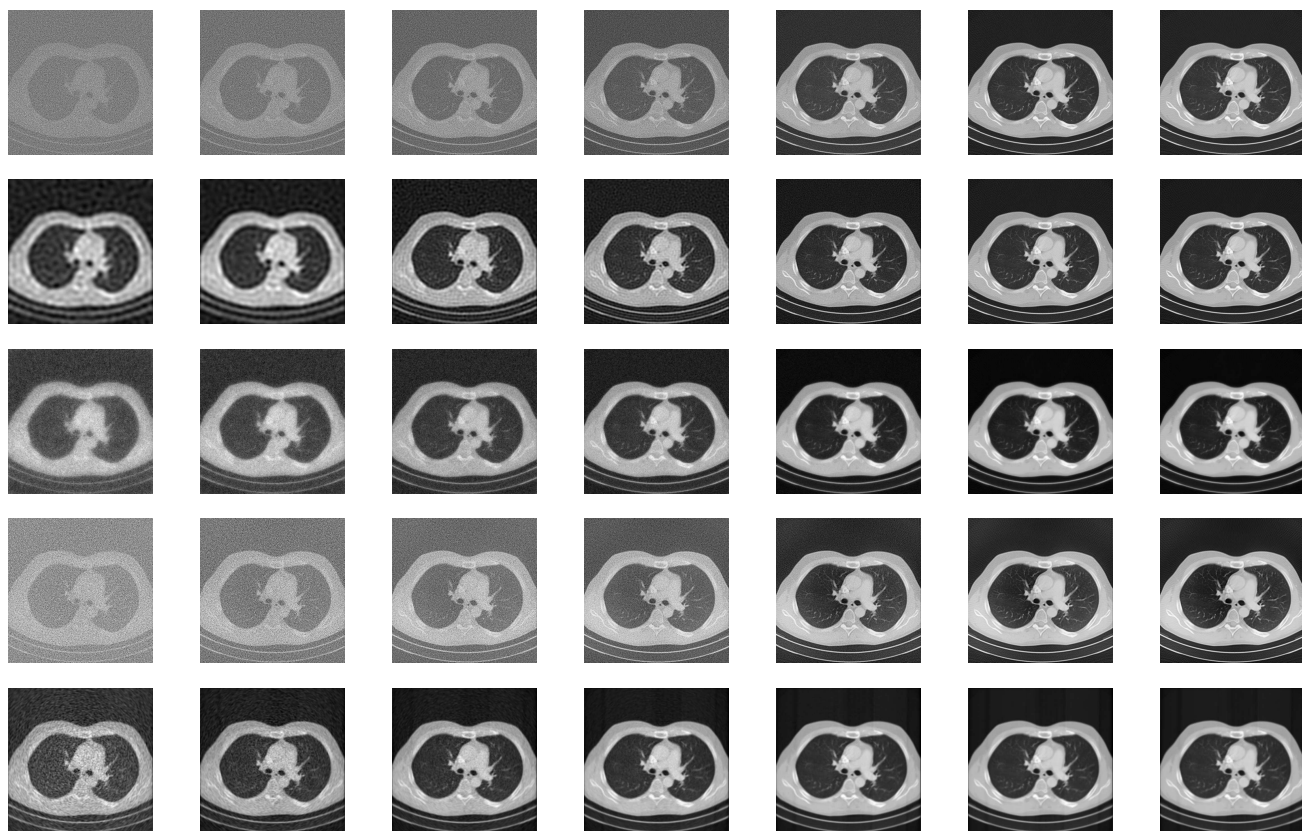


Fig. 4: Results with the third test image.

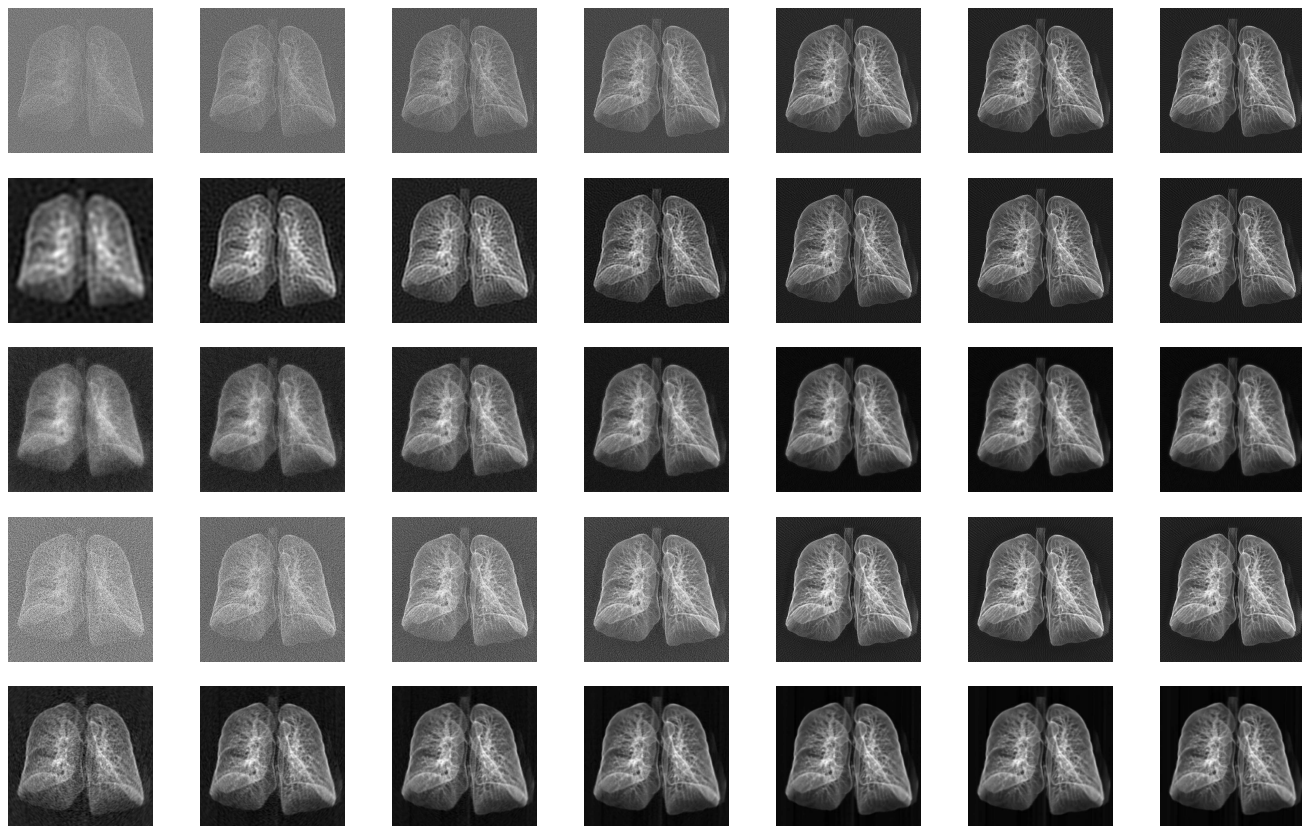


Fig. 5: Results with the fourth test image.

TABLE IV: MSEs and computation times with the fourth test image; each cell contains the MSE and the computation time (seconds, in parenthesis) averaged over ten replicated experiments.

SNR	25	30	40	50	60	70
oFBP (our method)	0.0180 (0.995)	0.0218 (0.494)	0.0124 (0.490)	0.0129 (0.490)	0.0112 (0.492)	0.0111 (0.506)
FBP	0.1419 (0.991)	0.1075 (0.496)	0.0517 (0.479)	0.0200 (0.485)	0.0156 (0.493)	0.0152 (0.490)
SIRT	0.0358 (32.625)	0.0268 (30.880)	0.0112 (52.103)	0.0070 (52.339)	0.0065 (51.913)	0.0065 (51.984)
MR-FBP	0.1106 (13.134)	0.0816 (13.043)	0.0340 (13.024)	0.0114 (13.073)	0.0107 (13.091)	0.0103 (13.103)
SMF-FBP	0.0205 (5.449)	0.0121 (2.940)	0.0074 (2.969)	0.0063 (2.953)	0.0062 (2.939)	0.0061 (2.993)

surprising that the FBP works worst for low SNR cases. Our oFBP suppresses the frequency bands of the projection data that contain significant noises, which improves the FBP in terms of noise handling capabilities. The MSE values of the oFBP is four to ten times smaller than those of the FBP. The computation times of the two methods are almost same, faster than the other compared methods.

6 and 7 compare the filters achieved by the oFBP with the Ram-Lak filter for the first and third test images under different SNRs. We can see that the oFBP algorithm zeros out most high frequency bands in the Ram-Lak filter. The choices of the suppressed frequency bands are dependent on the noise levels and the input data. The oFBP algorithm is adaptive to input data.

2) *oFBP* vs. *SIRT*: The SIRT is an algebraic method, which is generally believed working better with noisy data than the analytical method such as FBP. The overall accuracy of the oFBP is better than that of the SIRT for high noisy cases, which shows strong denoising capabilities of the oFBP. On the other hand, the oFBP spent much shorter time than the SIRT. Qualitatively, the reconstructed image by the oFBP is clearer than that by the SIRT. The MSE values of the oFBP are uniformly better than that of the SIRT except a few cases. The only exceptions are the cases with $\text{SNR} \geq 50$ for the first test image. The SIRT continue its iterations to minimize the mean projection error, which may result in overfitting to noisy data, while the overfit is reduced in our approach by regularizing the solution as we discussed in Section III.

3) *oFBP* vs. *MR-FBP*: The MR-FBP algorithm [12] optimizes the backprojection filter for minimizing the projection error of the reconstructed image. The MSE values of the MR-FBP algorithm is much better than the conventional FBP algorithm. However, as a by-product, it produces significant image artifacts, e.g. multiple vertical and horizontal lines starting from the center of reconstructed images to image borders for the first image. Our oFBP does not produce such artifacts. Moreover, we can see that MR-FBP performs poorly for low SNR cases, retaining observation noises heavily. The overall MSE performance of the oFBP outperforms that of the MR-FBP algorithm. The computation times of the two methods are not comparable, because our method is written in MATLAB while the author's code for the MR-FBP is written in Python.

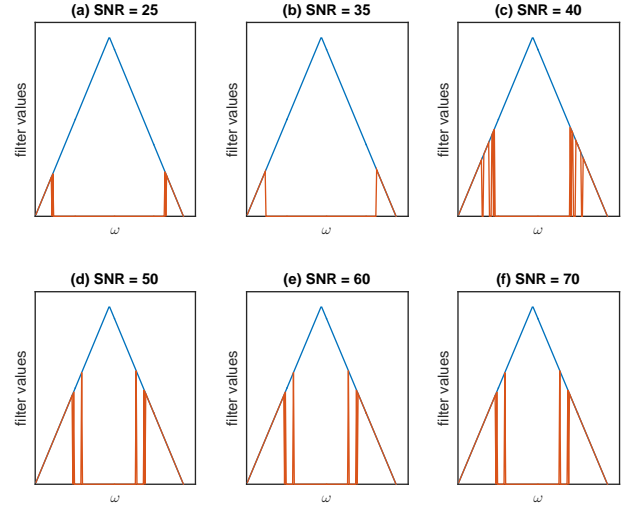


Fig. 6: The Ram-Lak filter (blue line) and the filter optimized by the oFBP (red line) for the first image under different SNR levels

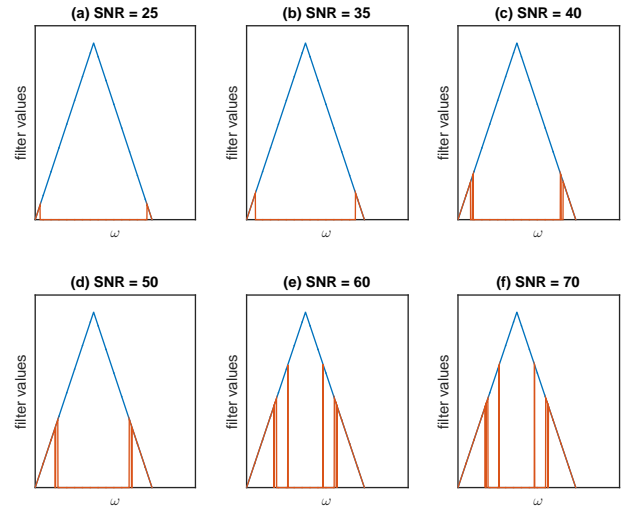


Fig. 7: The Ram-Lak filter (blue line) and the filter optimized by the oFBP (red line) for the third image under different SNR levels

4) *oFBP* vs. *SMF-FBP*: The SMF-FBP [15] mainly applies a special mean filter on the projection domain for denoising and then perform the conventional filtered backprojection on the denoised data. The SMF-FBP produces undesirable artifact. The artifacts look significant for the first test image as shown in 2. For the first test image, the SMF-FBP produces two white vertical lines that do not exist in the original image. Our oFBP method outperforms the SMF-FBP in both MSE and computation speed.

We also compared the five methods in terms of their reconstruction errors in each of the image background region and image foreground region. We applied a simple image

segmentation method to separate each of the first and third test images into foreground regions and background regions as shown in 8. We computed the average MSE values of each of the compared methods in the foreground regions and the background regions. Note that the two test images have flat backgrounds, so the noisy versions of them contains pure noises, not much signals. By looking at the MSE values in the background regions, we can judge the denoising capabilities of the compared methods. Tables V and VI summarizes the outcomes. We see that under all SNR levels, the MSE of the oFBP method for the backgrounds is the smallest, comparing with the other methods. This shows the excellence of oFBP method in denoising.



Fig. 8: The segmented first test image and third test image.

TABLE V: MSE of the compared methods in the background regions and the foreground regions for the first test image with SNR = 25

	Background MSE	Foreground MSE	Overall MSE
oFBP (proposed method)	0.0406	0.0835	0.0476
FBP	0.2029	0.0700	0.1812
SIRT	0.0677	0.0579	0.0661
MR-FBP	0.0741	0.1304	0.0833
SMF-FBP	0.0631	0.0086	0.0542

B. Comparison Under Missing Angles and Observation Noises

In practice, we cannot achieve projection data for a full range of 180 degree projection angles. In this section, we study how the five methods work when projection data are not available for some angles. For the study, we simulated projection data as in the previous section with SNR fixed to either 25 or 40 and removed a part of the projection data for some projection angles. The partial projection data was fed as inputs to each of the five compared methods. The resulting reconstructed images were compared with the groundtruth

TABLE VI: MSE of the compared methods in the background regions and the foreground regions for the third test image with SNR = 25

	Background MSE	Foreground MSE	Overall MSE
oFBP (proposed method)	0.0137	0.0131	0.0135
FBP	0.1380	0.0509	0.1070
SIRT	0.0444	0.0115	0.0327
MR-FBP	0.1348	0.0924	0.1197
SMF-FBP	0.0180	0.0236	0.0149

images, and the MSE values were computed. The range of the projection angles available to the methods varies is $[-r, r]$ degree with r varying in between 75 and 90.

The MSE performances of the five methods are summarized in 9 and 10. Under moderate noise (SNR=40), the SIRT performs best, while our approach is the second best but performs close to the SIRT. Under high noise level (SNR=25), our approach outperforms the SIRT. This shows that our proposed approach works well under both of noise scenarios and missing angle scenarios. 11 illustrates the reconstructed images of the five compared methods for the fourth test image with $r = 75$ and SNR=40. Under missing angles and the present of noises, we see that our proposed method still shows advance in the reconstructed images qualitatively, for a more detailed and accurate reconstruction. For example, in the test image 4, the finer details of the reconstruction in the image are very clearly shown.

VI. CONCLUSION

In this paper, we present an improvement of the filtered backprojection for tomography reconstruction. The new approach formulates an optimization problem that optimizes the backprojection filter to minimize the regularized reconstruction error. Solving the optimization can be achieved by a simple thresholding rule on the one-dimensional Fourier transform of projection data, so it is as fast as the conventional filtered backprojection. Since the approach seeks for the minimal reconstruction error, the reconstruction accuracy is great. We empirically showed that the accuracy of the proposed approach is superior to those of the algebraic methods and the most recent filtered backprojection methods, regardless of a full-angle tilt range case or missing angle cases. The solution approach is really simple. We believe the proposed approach would be very practical with those strengths. Although the approach was described for two-dimensional reconstruction problems, the general idea can be easily generalized to three-dimension tomographic reconstruction problems.

APPENDIX NOISE PATTERN ANALYSIS

In this section, we empirically show that observations noises existing in projection data are white Gaussian noises. To check this argument, we use experimentally obtained transmission electron tomography images of nanoparticles. The images consists of the projections from 103 different angles in between 70° to -70° . For one of the projections, see 12, which is the 64th projection image. From each of the 5th, 35th, 64th, and 96th projection images, we makes 3 image crops of the image background, which contains noises only. We analyze the distribution of the image pixel values in the image crops and also analyze the spatial autocorrelation of them. The distribution is shown in the form of a histogram in 13 and in the form of empirical cumulative distribution function (CDF) in 14-(a). The empirical CDF matches well to a Gaussian distribution. To check independence of the noises, we checked the spatial autocorrelation of the pixel values of the image crops. 14-(b) shows the autocorrelation values,

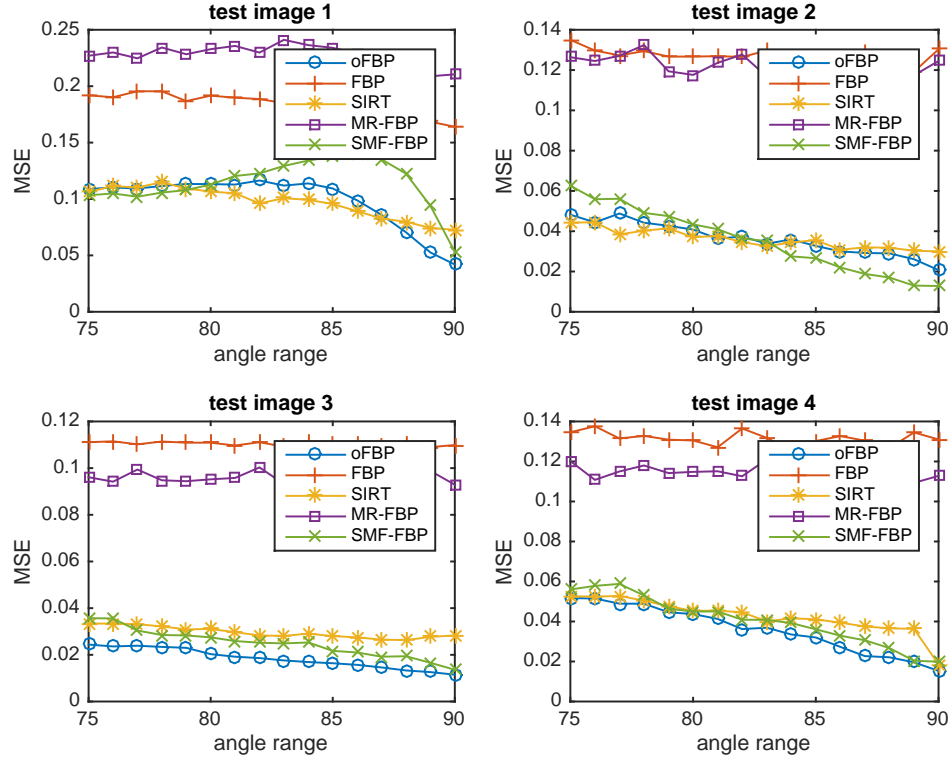


Fig. 9: MSE vs. range of available projection angles for the four test images and SNR = 25. The x-axis value r implies that the range of available projection angles is $[-r, r]$.

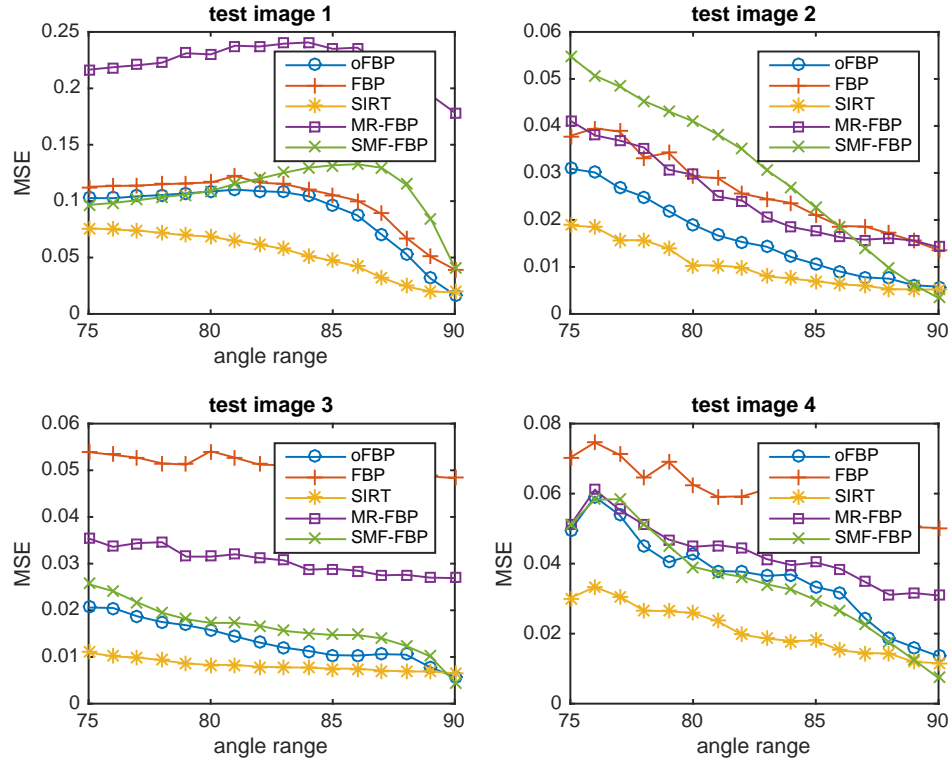


Fig. 10: MSE vs. range of available projection angles for the four test images and SNR = 40. The x-axis value r implies that the range of available projection angles is $[-r, r]$.

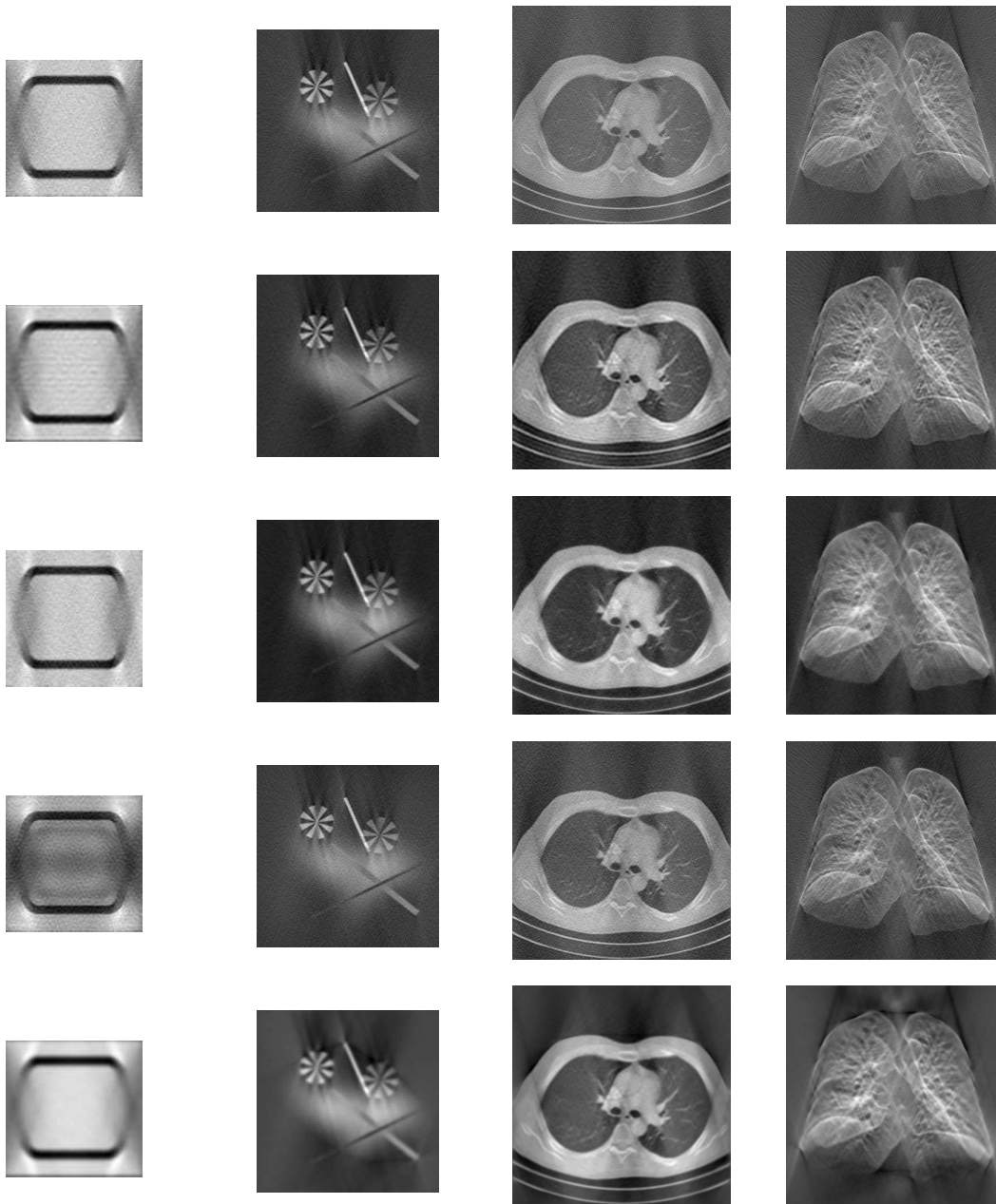


Fig. 11: Reconstruction under missing angle case for the angle range $(-75, 75)$ degree with $\text{SNR} = 40$. The first row through the fifth row of the images correspond the reconstruction results from the oFBP, oFBP, SIRT, MR-FBP and SMF-FBP method respectively.

which are around zeros. This implies the image noises are independent.

ACKNOWLEDGMENT

The authors would like to acknowledge support for this project. This work is partially supported by NSF 1334012, AFOSR FA9550-13-1-0075, AFOSR FA9550-16-1-0110, and FSU PG 036656.

REFERENCES

- [1] B. J. I. Günter Möbus, "Nanoscale tomography in materials science," *Materials Today*, vol. 10, pp. 18–25, 2007.
- [2] J. Frank, Ed., *Electron Tomography: Methods for Three-Dimensional Visualization of Structures in the Cell*. New York, NY, USA: Springer.
- [3] P. Grangeat and J.-L. Amans, Eds., *Three-Dimensional Image Reconstruction in Radiology and Nuclear Medicine (Computational Imaging and Vision)*. New York, NY, USA: Springer.
- [4] A. Kak and M. Slaney, *Principles of computerized tomographic imaging*. Philadelphia, PA, USA: Society of Industrial and Applied Mathematics, 2001.
- [5] X. Pan, E. Y. Sidky, and M. Vannier, "Why do commercial ct scanners still employ traditional, filtered back-projection for image reconstruction?" *Inverse Problems*, vol. 25, no. 12, pp. 421–434, 2009.
- [6] K. M. Hanson, *Radiology of the Skull and Brain, Vol. 5: Technical Aspects of Computed Tomography*. St. Louis, MO, USA: C. V. Mosby, 1981, ch. Noise and contrast discrimination in computed tomography.
- [7] R. Hegerl and A. S. Frangakis, *Electron Tomography: Methods for*

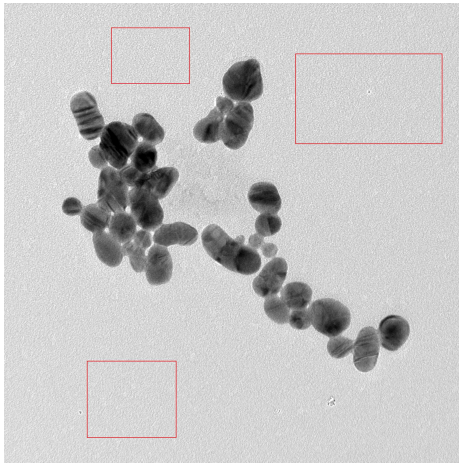


Fig. 12: Three image crops from the 64th projection image.

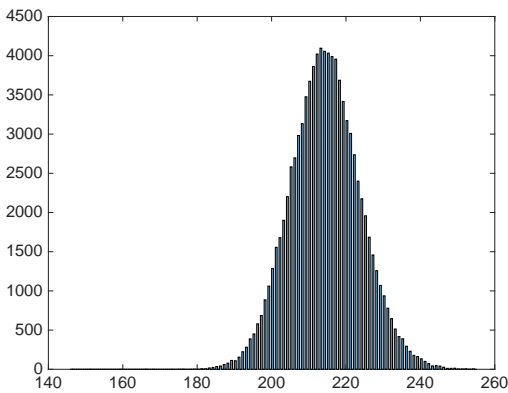
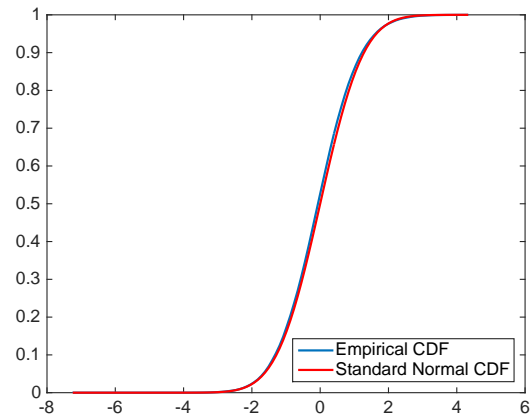
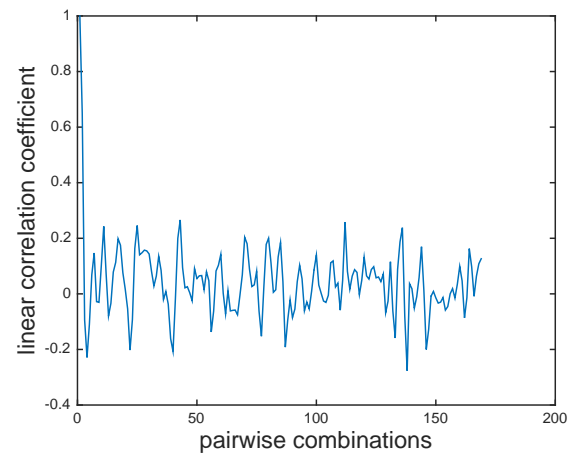


Fig. 13: The histogram of pixel values in the three crops from the 64th projection image.



(a) CDF



(b) Correlation

Fig. 14: Distribution and independence of noise pixel values. (a) The normalized CDF of background pixel values vs. standard Gaussian CDF; the image pixel values are normalized by dividing them by their standard deviation. (b) Spatial autocorrelation of the image pixel values from the three crops of the 64th projection image.

Three-Dimensional Visualization of Structures in the Cell. New York, NY, USA: Springer, 2006, ch. Denoising of Electron Tomograms.

- [8] R. Gordon, R. Bender, and G. Herman, "Algebraic reconstruction techniques (art) for three-dimensional electron microscopy and x-ray photography," *J. Theor. Biol.*, vol. 29, no. 3, pp. 471–476, 1970.
- [9] G. T. Herman, *Image Reconstruction from Projections: The Fundamentals of Computerized Tomography.* New York, NY, USA: Academic Press, 1980.
- [10] M. Jiang and G. Wang, "Convergence studies on iterative algorithms for image reconstruction," *IEEE Trans. Med. Imag.*, vol. 22, no. 5, pp. 569–579, 2003.
- [11] A. H. Andersen and A. C. Kak, "Simultaneous algebraic reconstruction technique (sart): A superior implementation of the art algorithm," *Ultrason. Imaging*, vol. 6, pp. 81–94, 1984.
- [12] D. M. Pelt and K. J. Batenburg, "Improving filtered backprojection reconstruction by data-dependent filtering," *IEEE Trans. Image Process.*, vol. 23, no. 11, pp. 4750–4762, 2014.
- [13] —, "Accurately approximating algebraic tomographic reconstruction by filtered backprojection," in *Proc. 13th International Meeting on Fully Three-Dimensional Image Reconstruction in Radiology and Nuclear Medicine*, Newport, Rhode Island, USA, 2015, pp. 158–161.
- [14] Z. Ren, G. Liu, and Z. Huang, "Study on an improved filtered back-projection image reconstruction algorithm combined with wavelet denoising," in *Proc. SPIE International Symposium on Photoelectronic Detection and Imaging*, vol. 8907, Beijing, China, 2013.
- [15] H. Qu, F. Xu, X. Hu, L. Wang, J. Zhao, and Z. Zhang, "A novel denoising method based on radon transform and filtered back-projection reconstruction algorithm," *Opt. Laser. Eng.*, vol. 50, no. 4, pp. 593–598, 2012.
- [16] P. Bühlmann and B. Yu, "Sparse boosting," *J. Mach. Learn. Res.*, vol. 7, pp. 1001–1024, 2006.
- [17] K. P. Burnham and D. R. Anderson, *Model Selection and Multimodel Inference: A Practical Information-Theoretic Approach*, 2nd ed. New York, NY, USA: Springer, 2002.
- [18] H. Akaike, "A new look at the statistical model identification," vol. 19, no. 6, 1974.
- [19] G. E. Schwarz, "Estimating the dimension of a model," vol. 6, no. 2, 1978.
- [20] [Online]. Available: http://users.telenet.be/alain.dens/Patient_info_CT_nl.html
- [21] [Online]. Available: <http://www.medicaldryfilm.com/sale-353761-high-sharpness-medical-x-ray-film-laser-konida-for-ct-dr.html>



Chen Mu (St. M' 15) is currently a PhD candidate in the Department of Industrial and Manufacturing Engineering at Florida State University. He receives a Master's from Central Michigan University in 2014 and a Bachelor's degree from North China University of Technology in 2010, both in Mathematics. His research interests include data mining and statistical machine learning, with a focus and application on the missing data problem in 3D tomographic reconstruction.



Chiwoo Park (St. M' 08, M'12) received B.S. in industrial engineering at Seoul National University and Ph.D. degree in industrial engineering at Texas A&M University in 2011. He is currently Assistant Professor in the Department of Industrial and Manufacturing Engineering at Florida State University and a principal investigator at High Performance Materials Institute. His research includes data analytics for science and engineering problems, especially image and functional data analytics in nanoscience and manufacturing engineering. His work is being supported by the National Science Foundation and the Air Force Office of Scientific Research. He received the best student paper award at IEEE Conferences on Automation Science and Engineering in 2008, the Ralph E. Powe Junior Faculty Award from the Oak Ridge Associated Universities in 2013, and the IIE best application paper in 2014. He is an active member of IIE, IEEE and INFORMS.